

See discussions, stats, and author profiles for this publication at: <https://www.researchgate.net/publication/334259896>

New Control Functionalities for Launcher Load Relief in Ascent and Descent Flight

Conference Paper · July 2019

CITATIONS

11

READS

557

3 authors:



Pedro Simplicio

European Space Agency

34 PUBLICATIONS 393 CITATIONS

SEE PROFILE



Andrés Marcos

Technology for Aerospace Control Ltd.

168 PUBLICATIONS 2,358 CITATIONS

SEE PROFILE



Samir Bennani

European Space Agency

157 PUBLICATIONS 1,603 CITATIONS

SEE PROFILE

New Control Functionalities for Launcher Load Relief in Ascent and Descent Flight*

Pedro Simplicio[†], Andrés Marcos* and Samir Bennani***

**Technology for Aerospace Control Lab, University of Bristol
University Walk, Bristol BS8 1TR, UK
pedro.simplicio/andres.marcos @bristol.ac.uk*

***GNC Section, European Space Agency
Keplerlaan 1, 2200 AG Noordwijk, NL
samir.bennani@esa.int*

[†]Corresponding author

Abstract

The development of effective load relief strategies is key to the improvement of launcher flight performance as it enables a joint increase of wind resilience and decrease of mass. This is particularly relevant for reusable launchers, which are aimed at maximising their operational availability and payload capacity. Yet, despite various advances in aeronautics and wind energy load relief, classical feedback-only techniques remain the state-of-practice for launchers. In this article, an improved load relief functionality is proposed by augmenting a conventional control design with a disturbance observer for on-board wind anticipation. Without requiring any change in the feedback loop, this approach also paves the way for the use of forward-looking wind estimation in the launcher domain. The disturbance observer is designed and analysed using robust control techniques for a lightweight, non-winged reusable launch vehicle, which relies on the use of planar fins for unpropelled descent attitude control. While the use of fins for launch is not a common practice, the article also exemplifies how their use can further improve launcher performance.

1. Introduction

The potential benefits and technical feasibility of launcher reusability as a key paradigm for sustainable access to space have been recently demonstrated by private companies (i.e. SpaceX and Blue Origin with the successful vertical take-off and vertical landing (VTVL) of reusable boosters²). In parallel, several programmes have been established with the objective of tackling the necessary maturation of descent and landing (D&L) technologies and reduction of launcher development and operation costs.^{6, 8, 20, 23}

As a supplement to these efforts, a European Space Agency (ESA) sponsored activity is studying how new guidance and control (G&C) functionalities can contribute to the aforementioned objective. In a previous work,¹⁸ an on-board convex optimisation-based recovery guidance algorithm specifically tailored to the extended flight envelope encountered by reusable launcher vehicles (RLVs) has been developed. That development relied on the assumption that attitude commands are perfectly followed so that attitude control has no impact on the trajectory.

The present article, on the other hand, is focused on the impact of attitude control on the loads experienced by RLVs and on how these loads can be minimised through proper control design. In particular, loads arising from the aerodynamic forces exerted on the vehicle must be maintained below certain safety limits for a set of admissible wind conditions. When load relief is not properly addressed at attitude control design stage, launcher manufacturers account for the safety limits by over-dimensioning the structure and constraining the admissible wind conditions. Hence, besides improving wind resilience, better load alleviation enables a decrease of structural mass, allowing an increase of payload mass and reduction of the launch cost per kilogram of payload.

Feedback-based design principles for load management are rooted on the work of Hoelker,¹⁰ who established a set of minimum error/drift/load control conditions, although it is well-known that achieving an acceptable compromise

*This work is funded by an ESA Networking Partnering Initiative (NPI) contract No. 4000119571/17/NL/MH with Dr. Stephan Theil (DLR Bremen) as project coordinator. Mr. Simplicio is also the recipient of a Doctoral Training Partnership award by the UK EPSRC.

between these competing conditions over the flight and for different launcher configurations is not straightforward.¹² More advanced methods have been proposed based on total angle of attack estimation,³ the adoption of a light detection and ranging (LiDAR) sensor for forward-looking wind information,^{5,13} and the use of adaptive control augmentation to recover performance in off-nominal conditions.¹⁵ Nonetheless, even though analogous developments have taken place, and are well advanced for operational deployment, in the fields of aeronautics^{7,9,16,22} and wind energy,^{11,24} the reliance on conventional control design principles remains the state-of-practice for launcher load relief.^{21,25}

The objective of this paper is to showcase a simple way to reconcile more conventional launcher control design approaches with the benefits of anticipating the contribution of wind on the load experienced by the vehicle. This is achieved first by augmenting a feedback-only architecture^{14,17} with a channel that provides information of wind disturbances, and then designing an observer to estimate those disturbances using robust control techniques,¹ here termed robust wind disturbance observer (rWDO).

The proposed approach is developed based on an RLV benchmark of a liquid-fuel VTVL booster used as first stage of a lightweight, non-winged launcher injecting a 1,100 kg satellite in a quasi-polar orbit at 800 km.¹⁹ The vehicle is steered via a thrust vector control (TVC) system, which is supplemented by two pairs of planar fins when the thrust level is low. Since most of the recovery phase is unpropelled, descent attitude control (and therefore load relief) relies extensively on the use of fins. Conversely, the use of fins during launch (where thrust level is very high) is not common practice, yet the article will show that further load relief improvements are possible by doing so. The study of the combined use of TVC and fins during descent flight is also particularly novel in launcher control literature. Descent flight control of a VTVL vehicle has been addressed by Boelitz,⁴ but only TVC was considered.

The paper begins with the introduction of the aforementioned RLV benchmark in Sec. 2, followed by an analysis of achievable load relief capabilities and consequent performance trade-offs in Sec. 3. The rWDO design approach is then presented in Sec. 4 and applied to ascent flight using TVC alone and combined fins/TVC in Sec. 5, as well as to descent flight in Sec. 6. Finally, the main conclusions are provided in Sec. 7.

2. Reusable Launcher Benchmark

This article relies on the nonlinear 6 degrees-of-freedom RLV benchmark developed by the authors¹⁹ to study the inherent couplings between reusable flight mechanics and G&C. It simulates the ascent, retro-propulsive descent and pinpoint landing of a liquid-fuel VTVL booster used as first stage of an axisymmetric vehicle launched from the European Space Centre in French Guiana to inject a 1,100 kg satellite in a quasi-polar orbit at 800 km. The vehicle is mainly steered via a TVC system, but two pairs of planar fins are included to provide attitude control under low thrust and two pairs of cold gas thrusters for low dynamic pressure conditions.

The benchmark includes standard algorithms for attitude control and open-loop trajectory for ascent guidance. This benchmark has been used to develop and verify an on-board convex optimisation-based guidance algorithm for the recovery phase, which is termed *DESCENDO*.¹⁸ Concerning the recovery, two distinct mission profiles can be studied: downrange landing, in which the RLV stage lands close to its unpropelled impact site, and return to launch site, where the stage uses an additional firing to return to its launch site. In order to define the guidance laws in the same way for both scenarios, the associated calculations are made in a recovery-pad reference frame. In both cases, a thrust vector is commanded by the guidance subsystem and then converted to reference pitch and yaw angles, θ_{ref} and ψ_{ref} , as well as thrust magnitude T_{ref} . In the present article, only downrange recovery is considered to simplify the presentation.

2.1 Linear RLV model

In an axisymmetric launcher with quasi-zero roll rate, pitch and yaw motions are often assumed uncoupled and the task of attitude control design and analysis can be performed in a single plane. The model of the vehicle in the pitch plane is depicted in Fig. 1. Since this article is dedicated to the study of atmospheric flight only, the use of cold gas thrusters is not accounted for in the study. In addition, the main focus is on the impact of uncertainties and wind disturbances on flight performance, hence the effects of actuator, sensor, bending and sloshing dynamics are not considered for the sake of simplicity.

For attitude control design and analysis, the motion of the RLV is described by a linear time-invariant (LTI) perturbation model $G_{\text{RLV}}(s)$, obtained by linearising the nonlinear equations of motion and defined as:

$$\begin{bmatrix} \dot{\theta} & \ddot{\theta} & \dot{z} & \ddot{z} \end{bmatrix}^T = A_{\text{RLV}} \begin{bmatrix} \theta & \dot{\theta} & z & \dot{z} \end{bmatrix}^T + B_{\text{RLV}} \begin{bmatrix} \mathbf{u} \\ v_w \end{bmatrix} \quad (1)$$

where θ , $\dot{\theta}$ and $\ddot{\theta}$ represent pitch angle and first/second-order derivatives, z , \dot{z} and \ddot{z} are the lateral drift and derivatives, $\mathbf{u} = [\beta_{\text{TVC}} \ \beta_{\text{fin}}]^T$ represents TVC and fin control inputs respectively, and v_w is the wind disturbance speed. In this equation, matrices A_{RLV} and B_{RLV} are given by:

$$A_{RLV} = \begin{bmatrix} 0 & 1 & 0 & 0 \\ \mu_\alpha + \mu_f \cos \beta_{fin,0} & -\frac{l_\alpha \mu_\alpha + l_f \mu_f \cos \beta_{fin,0}}{V \cos \alpha_0} & 0 & \frac{\mu_\alpha + \mu_f \cos \beta_{fin,0}}{V \cos \alpha_0} \\ 0 & 0 & 0 & 1 \\ -\frac{N_\alpha + N_f \cos \beta_{fin,0}}{m} - a_x & \frac{l_\alpha N_\alpha + l_f N_f \cos \beta_{fin,0}}{m V \cos \alpha_0} + v_x & 0 & -\frac{N_\alpha + N_f \cos \beta_{fin,0}}{m V \cos \alpha_0} \end{bmatrix} \quad (2)$$

$$B_{RLV} = \begin{bmatrix} 0 & 0 & 0 \\ -\mu_c \cos \beta_{TVC,0} & -\mu_f \cos \beta_{fin,0} & -\frac{\mu_\alpha + \mu_f \cos \beta_{fin,0}}{V \cos \alpha_0} \\ 0 & 0 & 0 \\ -\frac{T}{m} \cos \beta_{TVC,0} & \frac{N_f}{m} \cos \beta_{fin,0} & \frac{N_\alpha + N_f \cos \beta_{fin,0}}{m V \cos \alpha_0} \end{bmatrix} \quad (3)$$

in which aerodynamic, fin and TVC moment and force coefficients are defined as:

$$\mu_\alpha = \frac{N_\alpha}{J_N} l_\alpha, \quad N_\alpha = QS_{ref} C_{N_\alpha}, \quad \mu_f = \frac{N_f}{J_N} l_f, \quad N_f = 2QS_{fin} C_{f_\alpha}, \quad \mu_c = \frac{T}{J_N} l_c \quad (4)$$

with $l_\alpha = x_{CP} - x_{CG}$, $l_f = x_{fin} - x_{CG}$ and $l_c = x_{CG} - x_{PVP}$. The trim velocity and acceleration are generically given by:

$$v_x = V \cos \alpha_0, \quad a_x = g \sin \theta_0 \quad (5)$$

but during ascent flight (and only) the equations of motion can be linearised around a gravity turn trajectory and these terms simplify into:

$$v_x = 0, \quad a_x = \frac{T \cos \beta_{TVC,0} - A}{m} \quad (6)$$

In this specific case, this model corresponds to the one employed in previous works,^{14,17} although no fins were considered before and it was further assumed that $\alpha_0 \approx \beta_{TVC,0} \approx 0$.

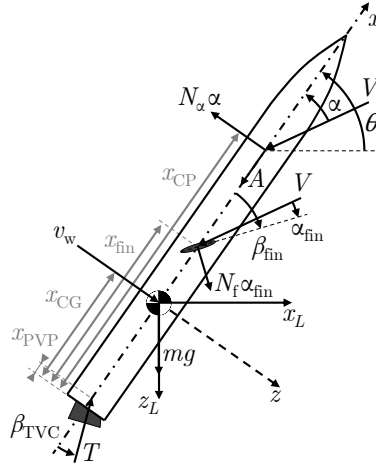


Figure 1: RLV model diagram

The aerodynamic load generated by the vehicle is directly proportional to the angle of attack (AoA) α , hence the following equation is also necessary to provide a point-mass load indication at its centre of gravity (CG):

$$\alpha = \theta + \frac{\dot{z} - v_w}{V \cos \alpha_0} \quad (7)$$

Nominal values of all the required variables are extracted from the RLV benchmark for two flight time instances, one during ascent and the other during descent, see Table 1. In addition, parametric uncertainties are introduced in the linear fractional transformation (LFT) form,¹ similar to reference,¹⁷ and encapsulated in the uncertainty block:

$$\Delta_{RLV}(s) = \text{diag} \left[\mathbb{I}_6 \delta C_{N_\alpha}, \mathbb{I}_6 \delta C_{f_\alpha} \cos \beta_{fin}, \mathbb{I}_4 \delta Q, \mathbb{I}_2 \delta T \cos \beta_{TVC}, \mathbb{I}_8 \delta V \cos \alpha, \delta a_x, \mathbb{I}_6 \delta x_{CP}, \mathbb{I}_9 \delta x_{CG}, \mathbb{I}_6 \delta m, \mathbb{I}_3 \delta J_N \right] \quad (8)$$

As indicated in Table 1, an uncertainty range of 20% is assumed for aerodynamic-related parameters, 2% for mass, CG and inertia and 10% for the remaining variables. It is noted that the thrust force T , although commanded externally by the guidance subsystem as T_{ref} , is also modelled as an uncertain parameter for control design and analysis.

Table 1: Model parameters and uncertainty ranges at ascent and descent design points

Variable	Symbol	Units	Nominal ascent	Nominal descent	Uncertainty
Normal RLV force gradient	C_{N_α}	—	2.007	-2.963	20%
Normal fin force gradient	$C_{f_\alpha} \cos \beta_{fin,0}$	—	6.000	-5.583	20%
Dynamic pressure	Q	kPa	52.48	7.835	20%
Normal thrust force	$T \cos \beta_{TVC,0}$	kN	2386	49.69	10%
Longitudinal velocity	$V \cos \alpha_0$	m/s	571.4	-175.0	10%
Longitudinal acceleration	a_x	m/s ²	7.122	9.331	10%
Longitudinal CP coordinate	x_{CP}	m	18.36	5.317	10%
Longitudinal CG coordinate	x_{CG}	m	8.919	4.452	2%
Total RLV mass	m	kg	93.5×10^3	8.49×10^3	2%
Normal RLV moment of inertia	J_N	kg.m ²	46.0×10^5	0.64×10^5	2%
Reference RLV area	S_{ref}	m ²	7.14	7.14	—
Reference fin area	S_{fin}	m ²	0.54	0.54	—
Fin pivot point coordinate	x_{fin}	m	11.1	11.1	—
TVC pivot point coordinate	x_{PVP}	m	0.96	0.96	—

3. Achievable Load Relief Performance

Launcher missions impose a challenging set of requirements to the flight control system,¹⁷ including: (i) stabilising the vehicle and ensuring adequate gain and phase margins in nominal and dispersed conditions, (ii) tracking attitude commands with an error that converges to zero, (iii) attenuating induced aerodynamic loads and drift from the reference trajectory, (iv) minimising control actuation, and (v) rejecting disturbances such as wind gusts and internal dynamics.

These requirements are well-known to be competing: for example, load minimisation involves keeping the angle of attack small by pitching into the wind field, which necessarily causes attitude errors to grow. Hence, a successful control design must be able to exploit the underlying trade-offs while operating as close to the limits of performance as possible. This interplay is illustrated by the Pareto front in Fig. 2a. The achievable performance is determined both by the sophistication of the adopted controller and by the physical limitations of the system (e.g. an attitude correction using TVC will always generate a certain level of drift as a result of its side-force).

Control design becomes even more challenging because the wide flight envelope variation over the mission makes the limits of performance change and requires different control priorities. For instance, load relief (LR) is critical in regions of high dynamic pressure but not near touchdown, where the priority is to minimise tracking errors. The evolution of dynamic pressure and Mach number along the trajectory used in this work is shown in Fig. 2b. This plot also identifies the two flight instances introduced in the previous section. The ascent design point coincides with the launch peak of dynamic pressure and the other one with a 12 deg angle of attack retro-propulsive altitude reduction.

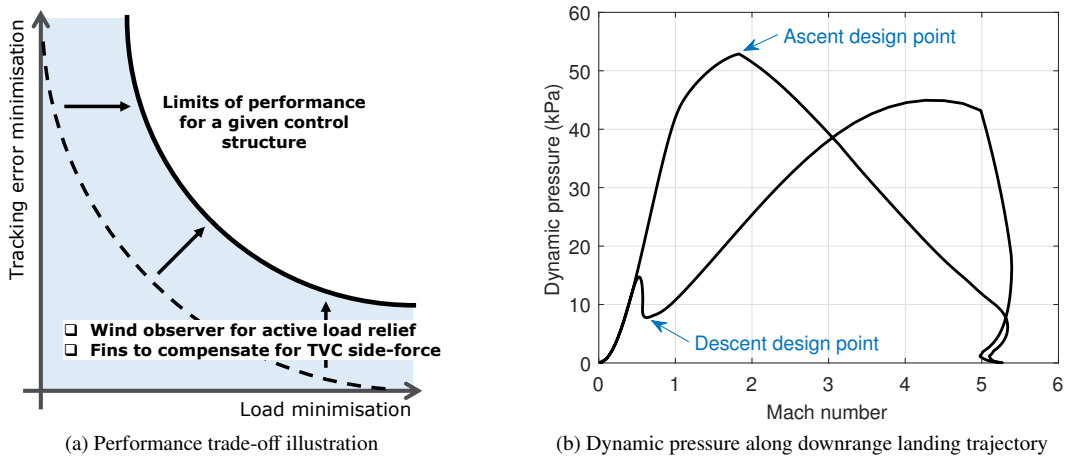


Figure 2: Main drivers of RLV control requirements

3.1 Proposed control functionalities

In this article, two control functionalities are proposed to enlarge the limits of performance (i.e. illustrated by the shift from the dashed line to the solid line in Fig. 2a).

The first functionality consists of augmenting a feedback-only architecture with a channel that provides information of wind disturbances and employ an observer to estimate those disturbances. This allows to enhance wind rejection without compromising nominal stability and tracking properties. The second functionality relies on the use of fins to compensate for the TVC side-force and therefore enabling further improvements in LR. The use of fins is mandatory in descent flight but it is not a common practice during launch. As it will be shown, significant gains (with relatively minor costs) are possible by also using fins in this phase.

To achieve this, consider first the closed-loop block diagram of Fig. 3a. This diagram features the guidance subsystem and an LFT block composed of $G_{RLV}(s)$ and $\Delta_{RLV}(s)$, all introduced before in Sec. 2. In addition, a derivative filter $H_{deriv}(s)$ is included to differentiate pitch angle commands, as well as a Dryden filter¹⁷ $G_{wind}(s)$ to simulate the frequency content of wind disturbances v_w by colouring a white noise signal n_w . These filters are given by:

$$H_{deriv}(s) = \frac{s}{0.20s + 1}, \quad G_{wind}^{\uparrow}(s) = \frac{3.54}{s + 0.32}, \quad G_{wind}^{\downarrow}(s) = \frac{2.36}{s + 0.15} \quad (9)$$

where the subscripts \uparrow and \downarrow refer to the ascent and descent design points, respectively. The attitude control loop is closed using a conventional static feedback controller K_{FB} , which is fed by pitch angle and rate errors, θ_e and $\dot{\theta}_e$, as well as drift rate \dot{z} for drift and angle of attack (AoA) minimisation (recall Eq. (7)). This controller is tuned using structured \mathcal{H}_{∞} optimisation with constraints on the transfer functions $\theta_{ref} \rightarrow \{\theta_e, \theta, \dot{z}, \beta_{TVC}\}$ and $n_w \rightarrow \{\theta_e, \alpha\}$. Details on the design process are outside the scope of this paper, but the reader is referred to the work of Navarro-Tapia *et al.*¹⁴

Assuming that perfect wind knowledge is available, then this information could be employed in a feedforward manner, through K_{LR} (see Fig. 3a), to anticipate and compensate for the effect of wind. However, in practice the wind needs to be either measured or estimated. Wind measurements can be obtained with a LiDAR sensor at the expense of additional instrumentation complexity.¹³ Alternatively, an observer $L_w(s)$ can be included, see Fig. 3b, to provide wind disturbance estimates \hat{v}_w . Section 4 is dedicated to the design of the observer $L_w(s)$, but an analysis of the impact of K_{LR} on the achievable performance is presented next, in Sec. 3.2.

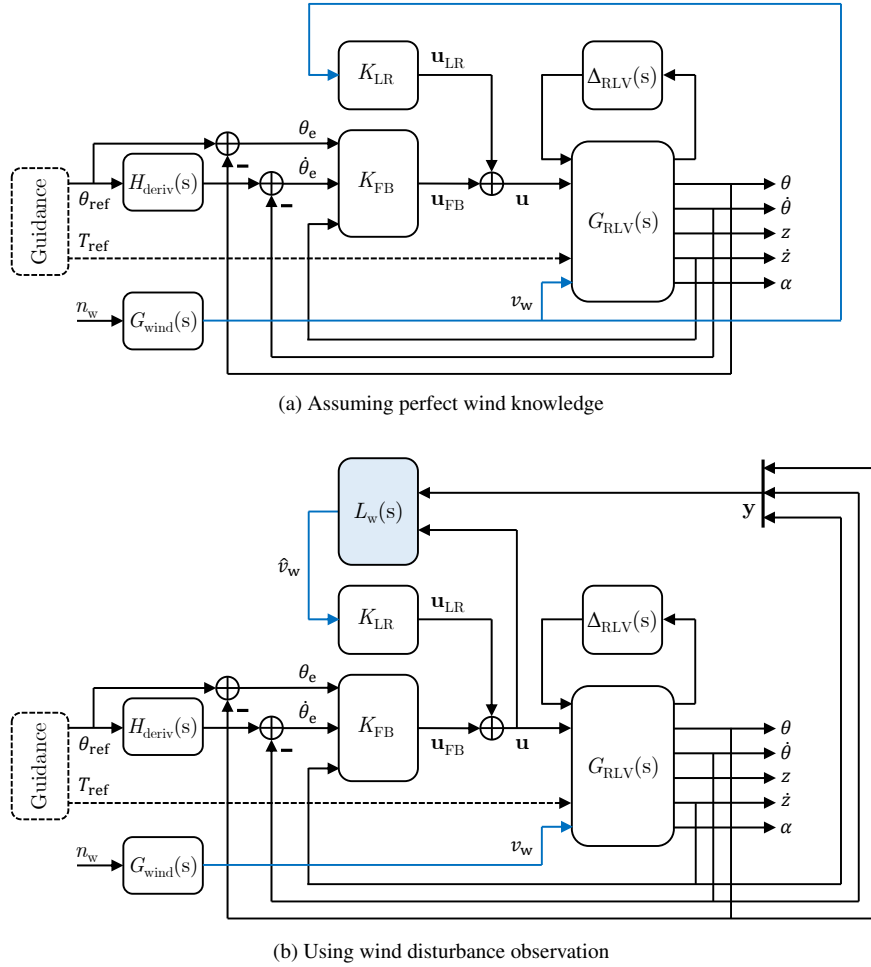


Figure 3: Closed-loop architecture with LR augmentation

3.2 Impact of wind anticipation

This analysis is based on the ascent design point with no fin control, for which the following feedback-only (FB-only) controller was designed (note that only 3 gains are used now):

$$K_{FB}^\dagger = \begin{bmatrix} -5.64 & -1.60 & 4.3 \times 10^{-4} \\ 0 & 0 & 0 \end{bmatrix} \quad (10)$$

The impact of K_{LR} can be appreciated by evaluating the system's response to a step signal in n_w . In this case, the states deviate from equilibrium in a monotonic manner, hence their value after a certain interval of time can be employed as a good indicator. The values of the most relevant variables after 6 seconds are shown in Fig. 4a using different colours. Here, K_{LR} represents a single gain from v_w to β_{TVC} , ranging from 0 (i.e. FB-only) to -0.015. In practice, more complex FB controllers can be used, e.g. dynamical ones, but to facilitate the understanding this simple case is chosen (especially since the conclusions are not invalidated by this assumption). The figure includes the indicators in nominal conditions ($\Delta_{RLV} = 0$) using solid lines and the worst corner-case (WC) from the LFT using dashed lines.

From Fig. 4a, distinct values of K_{LR} for minimum attitude error, drift rate and AoA (i.e. load) can be identified. These minima are analogous to the well-known Hoelker conditions,¹⁰ but with the key difference that K_{LR} does not enter the feedback loop and thus nominal stability/tracking properties are not affected. This figure also reflects the performance compromises discussed above. These are then evidenced by the radar plots of Fig. 4b to 4d, in which the FB-only indicators are compared to those obtained using the various minimum conditions. These radar plots show that each minimum condition optimises the corresponding indicator in both nominal and worst cases at the expense of degrading one of the others. Of special relevance for this work, Fig. 4d demonstrates that a direct trade-off between load relief and tracking error minimisation can be achieved.

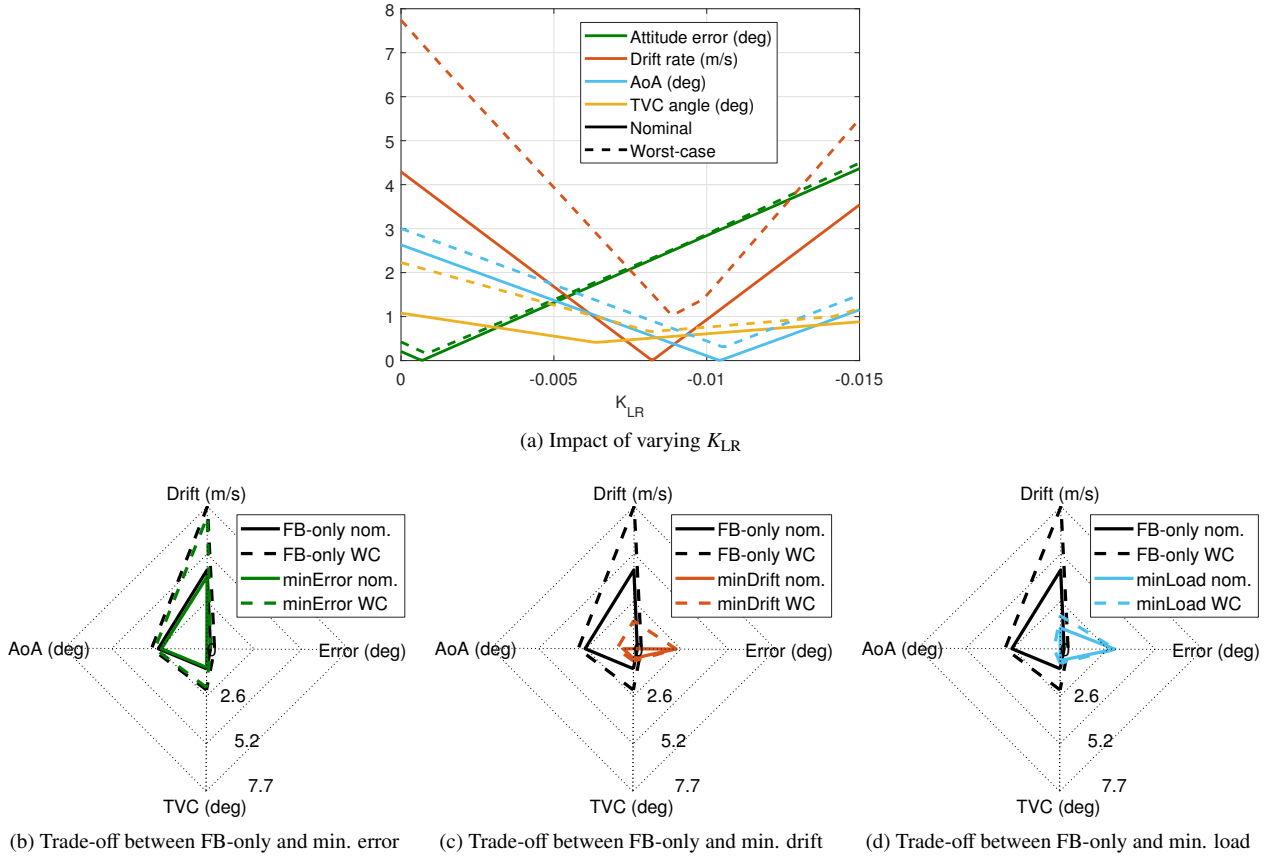


Figure 4: Wind step indicators

4. Robust Wind Disturbance Observer Design

This section is focused on the synthesis of the wind disturbance observer (WDO) $L_w(s)$, introduced in Fig. 3b. As depicted in that figure, $L_w(s)$ uses as inputs the feedback variables $\mathbf{y} = [\theta \ \dot{\theta} \ \dot{z}]^T$ and the control inputs $\mathbf{u} = [\beta_{TVC} \ \beta_{fin}]^T$ to provide wind disturbance estimates \hat{v}_w . The ascent point is again adopted for exemplification purposes in this section.

4.1 Problem formulation

A robust WDO (here termed rWDO) must fulfil the following requirements: (i) \hat{v}_w shall tend to zero in the absence of wind so that nominal stability/tracking properties of the system are not altered, (ii) \hat{v}_w shall tend to v_w so that the wind is accurately estimated, and (iii) the former two requirements shall hold for all the allowable control inputs \mathbf{u} and uncertainties Δ_{RLV} of Eq. (8). More formally, the design problem consists of finding an observer $L_w(s)$ such that:

$$\hat{v}_w(s) = L_w(s) \begin{bmatrix} \mathbf{y}(s) \\ \mathbf{u}(s) \end{bmatrix} \approx \begin{cases} 0, & v_w(s) = 0 \\ v_w(s), & v_w(s) \neq 0 \end{cases} \quad \forall \{ \mathbf{u}(s), \Delta_{RLV}(s) \} \quad (11)$$

As a tentative solution, it is possible to estimate the wind by solving the equations of motion with respect to v_w . For instance, inverting the pitch dynamics (second row of Eq. (1)) yields:

$$L_w^0(s) = \frac{V \cos \alpha_0}{\mu_\alpha + \mu_f \cos \beta_{fin,0}} \left[\begin{array}{c} \mu_\alpha + \mu_f \cos \beta_{fin,0} \\ -\frac{s}{\sigma_d s + 1} - \frac{l_\alpha \mu_\alpha + l_f \mu_f \cos \beta_{fin,0}}{V \cos \alpha_0} \\ \frac{\mu_\alpha + \mu_f \cos \beta_{fin,0}}{V \cos \alpha_0} \end{array} \middle| \Gamma_{ctr} \right] \quad (12)$$

in which $\sigma_d = 0.05$ is employed to make the differentiation proper and:

$$\Gamma_{ctr} = - \begin{bmatrix} \mu_c \cos \beta_{TVC,0} & \mu_f \cos \beta_{fin,0} \end{bmatrix} \quad (13)$$

is the control moment effectiveness matrix. The zero of Eq. (12) determines the frequency at which wind anticipation starts. This approach, however, presents severe robustness problems. To clearly understand them, it is convenient to reformulate the design problem using the robust control framework, see Fig. 5a.

The block diagram in Fig. 5a is obtained by rearranging the closed-loop interconnections of Fig. 3b so that the requirements of Eq. (11) can be assessed. This involves adding the output (error) signal $w_e = v_w - \hat{v}_w$ to quantify the observation mismatch. In addition, the impact of guidance commands is accounted for through a new input signal \mathbf{u}_{pert} acting as a perturbation on the control inputs, while the impact of wind is assessed through the same input n_w as before. It is also noted that the feedback controller K_{FB} must be included when performing the rWDO design, otherwise $G_{RLV}(s)$ and the whole closed-loop could not be stabilised.

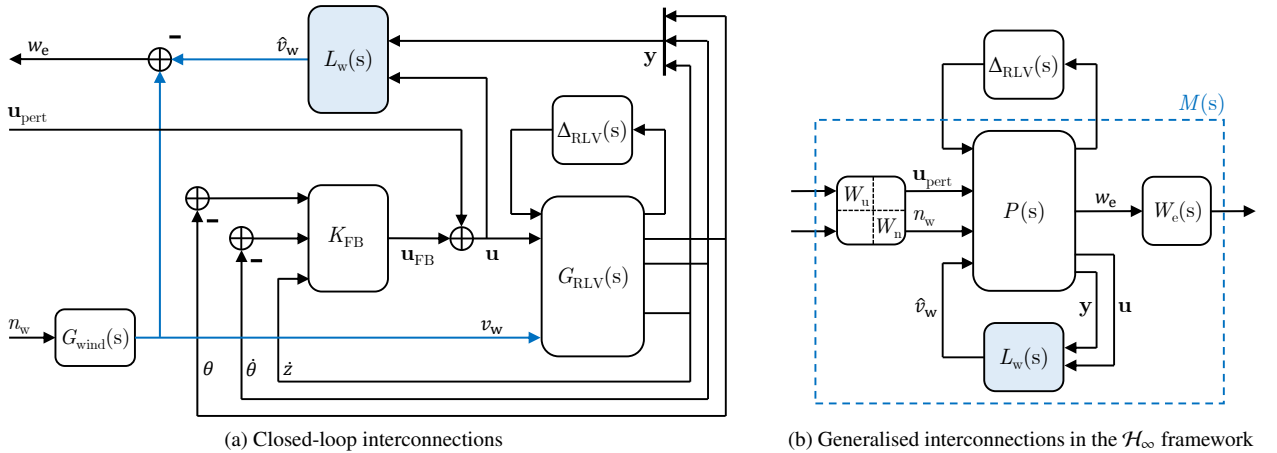


Figure 5: Closed-loop model for rWDO design

The input/output singular values of Fig. 5a, with $L_w^0(s)$ from Eq. (12) as WDO, are depicted in Fig. 6 using solid black lines. This figure shows that $L_w^0(s)$ is capable of ensuring a small observation error in the face of wind (right plot), i.e. the solid black line is below 0 dB. But, as seen respectively in the left and mid plots, this is not the case in the presence of TVC and fin perturbations, particularly at frequencies higher than 1 rad/s. On the other hand, at lower frequencies, an unnecessary roll-off is provided in the three channels. This indicates that there is potential to improve the observer by reshaping these frequency responses, for which \mathcal{H}_∞ optimisation¹ is an extremely suitable tool.

4.2 \mathcal{H}_∞ WDO synthesis

To tackle this problem, Fig. 5a is further rearranged into the interconnections of Fig. 5b, in which the same inputs/outputs, uncertainty block $\Delta_{RLV}(s)$ and WDO $L_w(s)$ can be identified. All the other elements are encapsulated in a generalised plant $P(s)$. As shown in Fig. 5b, this system is input/output weighted by W_u , W_n and $W_e(s)$, which specify the desired design requirements, forming the augmented plant $M(s)$. The \mathcal{H}_∞ problem then consists of finding an observer $L_w^*(s)$ that minimises the \mathcal{H}_∞ -norm of $M(s)$:

$$\min_{L_w(s)} \gamma = \|M(s)\|_\infty \quad (14)$$

which corresponds mathematically to minimising its maximum singular value (MSV), and physically to its worst-case input/output energy amplification. This problem, however, does not allow to specify the structure of $\Delta_{RLV}(s)$.

In practice, W_u and W_n are applied to define the expected range of \mathbf{u}_{pert} and n_w , and $W_e(s)$ normalises the system so that the MSV of $M(s)$ is bounded by $W_e^{-1}(s)$ if $\gamma < 1$. The advantage of having the initial guess $L_w^0(s)$ is related to the insight it provides when choosing a reasonable $W_e^{-1}(s)$ specification (see Fig. 6). More specifically, $W_e(s)$ is tailored to have: (i) a maximum value of $1/0.6$ so that the worst-case observation error is approximately the same as $L_w^0(s)$, (ii) a zero at 80 rad/s so that the observation bandwidth is also the same, and (iii) a pole 10^4 times faster to make the transfer function proper. These considerations lead to the following weights:

$$W_u = \frac{\pi}{180} \begin{bmatrix} 1 & 0 \\ 0 & 20 \end{bmatrix}, \quad W_n = 3, \quad W_e(s) = \frac{1}{0.6} \frac{s + 80}{s + 80 \times 10^4} \times 10^4 \quad (15)$$

Here, the input weights W_u and W_n are constant so as to minimise the order of the system, but frequency-dependent functions can also be considered.

With the above choice of weights, the \mathcal{H}_∞ synthesis problem yielded a stable 5th-order observer with the fastest pole below 90 rad/s and an optimal performance of $\gamma = 0.43$. The frequency-dependent requirement imposed by $W_e^{-1}(s)$ and the singular values attained with the latter observer are included in Fig. 6 using black dashed and red lines.

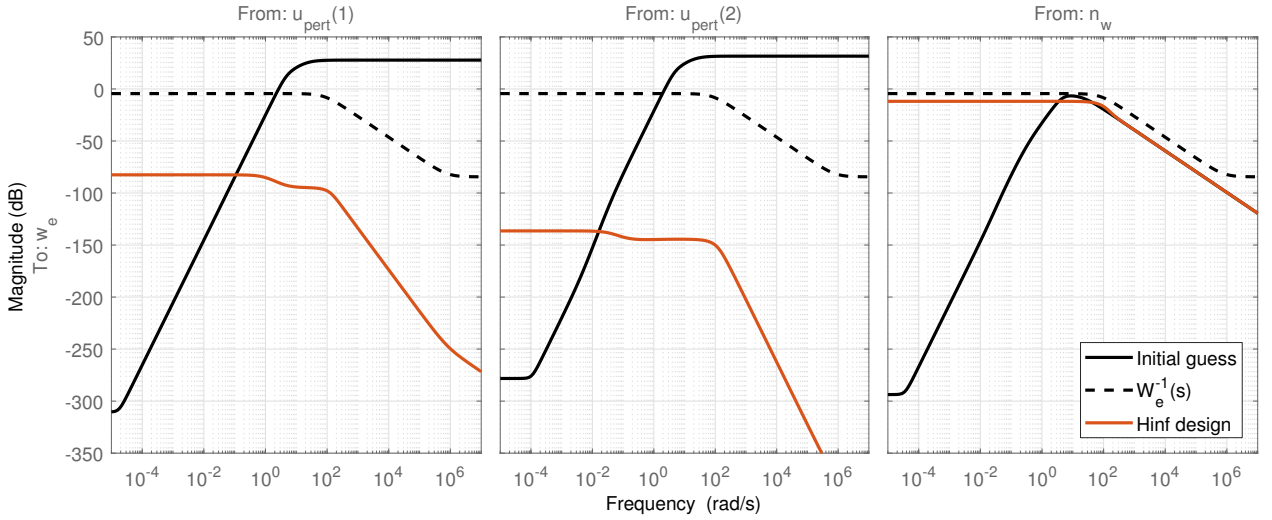


Figure 6: Multi-channel closed-loop singular values and requirement $W_e^{-1}(s)$

Comparing the \mathcal{H}_∞ design with the initial guess (the solid black lines in Fig. 6), it is clear that the optimised observer is able to effectively reject input perturbations (particularly at higher frequencies) at the expense of a larger steady-state error, which is bounded to $W_e^{-1}(0)/W_n = 20\%$. To verify whether this behaviour holds in the face of launcher uncertainties (recall Eq. (11)), structured singular value (SSV) analysis can now be employed.

The fundamental approach for analytical robustness assessment is based on the SSV μ .¹ Smaller values of $\mu \in \mathbb{R}^+$ indicate better robustness properties and system stability is guaranteed for all $\Delta_{RLV}(s)$ if and only if $\mu < 1$ over the frequency. The smallest norm of the worst-case set of uncertainties is then given by $\|\mu\|_\infty^{-1}$. In addition, this type of analysis allows to calculate the sensitivity of the μ solution with respect to each element of $\Delta_{RLV}(s)$. The computation of μ is polynomial-time hard, hence its estimation relies on lower and upper bounds.

The top plot of Fig. 7 depicts the bounds of μ for the system of Fig. 3b with $K_{LR}^* = -1.04 \times 10^{-2}$ for load minimisation (recall Fig. 4a) and with the \mathcal{H}_∞ -designed observer in red (solid line for upper bound and dashed for lower bound). The aforementioned sensitivities are shown in the bottom plot using a different colour for each uncertainty of Table 1. In the top plot, a peak of $\mu > 1$ indicating lack of robust stability (RS) can be seen for the \mathcal{H}_∞ design. From the bottom plot, it is possible to recognise the thrust uncertainty ($\delta T \cos \beta_{TVc}$) as the main responsible for this degradation.

4.3 D-K iteration WDO synthesis

To prevent the lack of RS, a new observer is designed using the so-called *D-K* synthesis algorithm,¹ which employs a combination of \mathcal{H}_∞ synthesis and μ analysis to account for the elements of $\Delta_{RLV}(s)$. Design weights are kept the same as for the \mathcal{H}_∞ design, but critically, only the thrust uncertainty is considered in the LFT model used for *D-K* synthesis. This is done in order to minimise the complexity of the problem and driven by the μ analysis results.

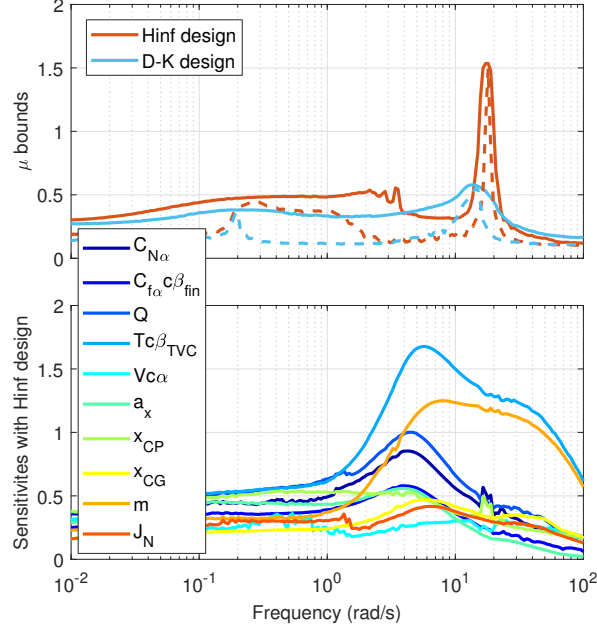


Figure 7: Robust stability upper and lower bounds (top plot) and sensitivities (bottom plot)

Following this approach, the D - K synthesis problem yielded an observer of the same order as before, with the fastest pole also below 90 rad/s and with an optimal performance of $\gamma = 0.58$. The bounds of μ obtained with this new observer are also shown in the top plot of Fig. 7 (blue lines), indicating that μ is now smaller than 1 for all the frequencies. This means that accounting for the impact of thrust changes in the synthesis process is enough to design an observer that is robust in the face of all the uncertainties $\Delta_{RLV}(s)$.

To clarify how the three WDOs ($L_w^0(s)$, the \mathcal{H}_∞ and D - K designs) differ from each other, their MSV are provided in Fig. 8a and the closed-loop pole dispersion generated with 500 random $\Delta_{RLV}(s)$ samples are depicted in Fig. 8b.

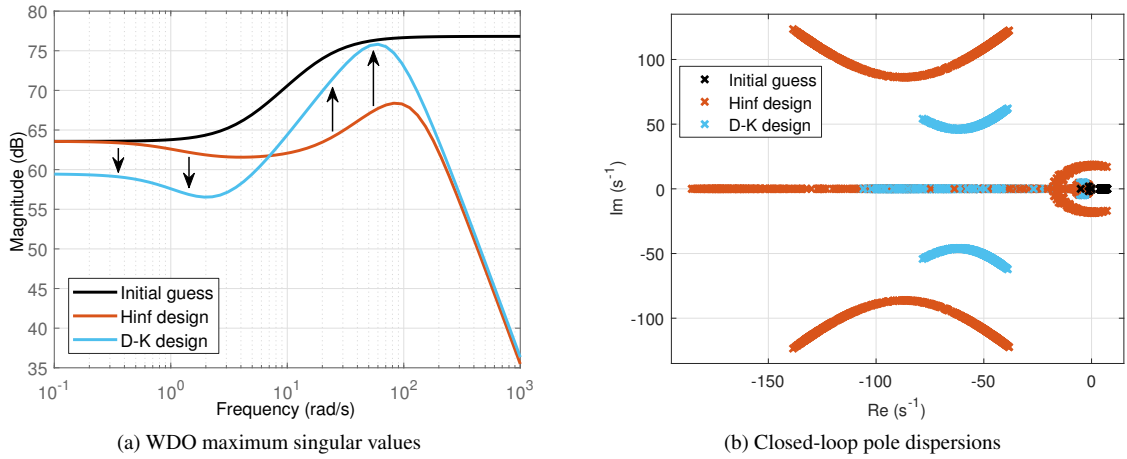


Figure 8: WDO design evolution

The initial guess $L_w^0(s)$ provides the desired wind anticipation action between 1 and 100 rad/s (Fig. 8a), but results in most configurations being unstable (notice the black positive poles in Fig. 8b). The \mathcal{H}_∞ -designed WDO (red colour) keeps the same steady-state gain as the initial guess (see Fig. 8a) but introduces a high-frequency roll-off that enables the rejection of input perturbations, at the expense of a higher order system. Although it stabilises most of the cases, a few of them remain unstable, as observed in Fig. 8b and identified by the peak of $\mu > 1$ in Fig. 7.

A robust disturbance observation is only ensured by the D - K design (blue colour), which effectively shrinks the pole dispersion to remain inside the left complex half-plane. This is achieved by relying less on low-frequency information and more on higher frequencies (as indicated by the arrows in Fig. 8a), while maintaining the roll-off of the \mathcal{H}_∞ design. The reduced confidence in low-frequency information when the thrust uncertainty is considered for the D - K design is consistent with the fact that this variable determines mostly the slower dynamics of the system.¹⁷ The application of the rWDO design approach to ascent and descent flight is further detailed in Sec. 5 and 6, respectively.

5. Application to Ascent Flight

The application and benefits of the functionalities proposed in Sec. 3.1 during ascent flight are demonstrated throughout this section using four controllers designed following different strategies (the indicated colours are used in the subsequent comparison plots):

1. In black, the TVC-only controller with the 3 non-zero gains of Eq. (10) and $K_{LR}^\dagger = \begin{bmatrix} 0 & 0 \end{bmatrix}^T$, i.e. with FB-only control.
2. In blue, a TVC-only controller augmented with the rWDO designed in Sec. 4.3, in which K_{FB}^\dagger and K_{LR}^\dagger are jointly tuned using structured \mathcal{H}_∞ optimisation. The achievable LR performance identified in Sec. 3.2 is employed as a tighter tuning requirement on the $n_w \rightarrow \alpha$ channel, allowing to recover the design of Sec. 4.3 in a methodical manner. The LR controller adds 1 extra gain (\hat{v}_w to β_{TVC}) to be tuned.
3. In red, a combined fins/TVC controller with $K_{LR}^\dagger = \begin{bmatrix} 0 & 0 \end{bmatrix}^T$ and with K_{FB}^\dagger tuned using structured \mathcal{H}_∞ optimisation. As anticipated in Sec. 3.1, fins can be used for load minimisation by counteracting the TVC side-force, which is enforced by augmenting the tuning requirements of the first controller with new constraints on the $\theta_{ref} \rightarrow \{\alpha, \beta_{fin}\}$ channels. The FB controller with combined fins/TVC has 6 gains to be tuned.
4. In green, a combined fins/TVC controller augmented with the rWDO designed in Sec. 4.3, in which K_{FB}^\dagger and K_{LR}^\dagger are jointly tuned using structured \mathcal{H}_∞ optimisation. Representing a combination of the last two strategies, this controller is generated using their respective $n_w \rightarrow \{\alpha, \beta_{fin}\}$ and $\theta_{ref} \rightarrow \{\alpha, \beta_{fin}\}$ requirements concurrently. The LR controller adds 2 extra gains (\hat{v}_w to β_{TVC} and to β_{fin}) to be tuned.

A comparative analysis of the frequency and time-domain properties obtained with these controllers is now provided in Sec. 5.1 and 5.2. The outcome of this comparison and the number of tunable gains is then summarised in Table 2.

5.1 Frequency-domain analysis

In the frequency-domain, the controllers are compared in nominal conditions using Nichols charts and in the face of uncertainties using μ analysis. For a detailed explanation of the application of these techniques to launcher flight control, the reader is referred to Simplicio *et al.*¹⁷

Nichols chart analysis is a single-channel tool, hence the closed-loop of Fig. 3b is first transformed as depicted in Fig. 9. This single-loop transformation uses the pitch control moment $m_{ctr} = \Gamma_{ctr} \mathbf{u}$ with Γ_{ctr} given by Eq. (13) and Γ_{ctr}^+ its pseudo-inverse matrix. The obtained Nichols charts are provided in Fig. 10a, where the resulting gain margin (GM) and phase margin (PM) are also indicated. The outcome of μ analysis is presented in Fig. 10b and is equivalent to that of the top plot of Fig. 7.

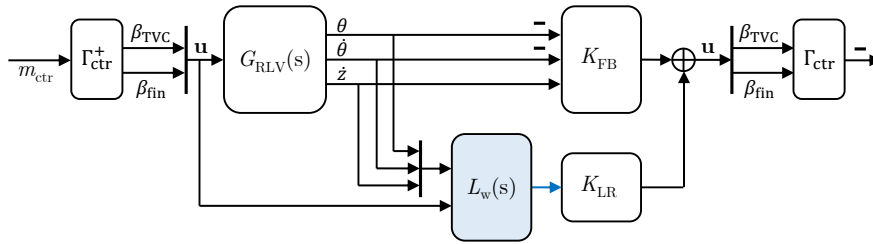


Figure 9: Loop transformation for Nichols chart generation

The first two controllers (both without including fin control, and respectively without and with rWDO) have the same gain and phase margins, as seen in Fig. 10a. This is because the observation error is zero in nominal conditions and the rWDO does not affect closed-loop stability. This is no longer the case in the face of uncertainties, as illustrated in Fig. 10b, where the presence of the rWDO in the second controller leads to an RS degradation (particularly around PM frequencies) due to delay added by the observer for wind estimation. This blue plot is the same as that of Fig. 7, and is repeated here for comparison of designs. Despite the RS degradation, the peak of $\mu = 0.53$ indicates that a very reasonable robustness margin is guaranteed to cover for effects that are not accounted for by the model (e.g. actuator and bending dynamics). This degradation is expected since the introduction of the WDO leads to a performance improvement that must be traded-off with robustness. Nonetheless, since the μ peak is still about 50% from the limit, this shows the room for improvement (without unacceptable robustness loss) that can be achieved with these techniques.

The red controller (fin control, without rWDO) yields a completely different frequency response, with smaller GM but larger PM, as shown by the Nichols chart. As it will be seen in Sec. 5.2, these differences are reflected in an improved command tracking response. In terms of RS, μ analysis identifies a slight degradation with respect to the TVC-only controller (in black), but much larger margins compared to the one without fins but with rWDO (in blue).

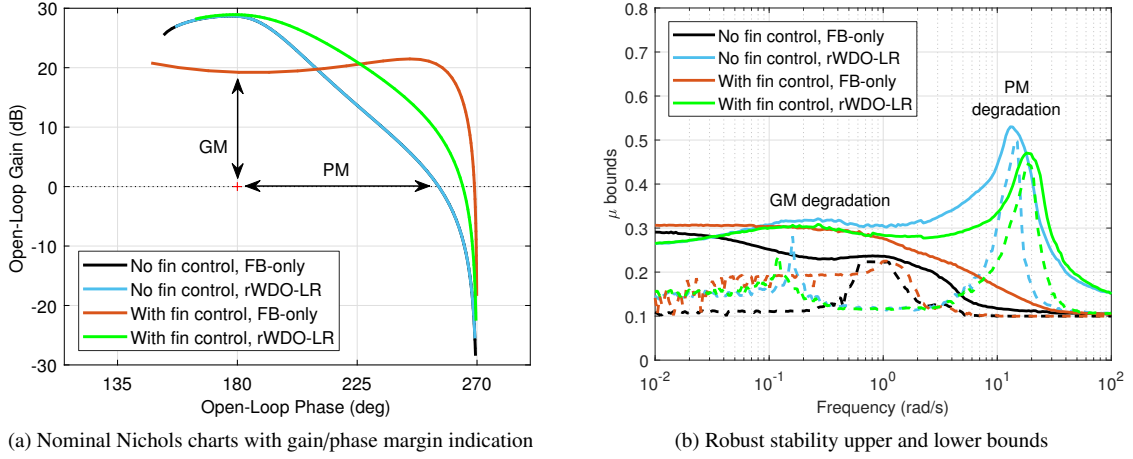


Figure 10: Frequency-domain comparison of ascent control functionalities

Finally, the inclusion of the rWDO with the fins (green lines) leads to smaller phase and RS margins. Nonetheless, the rWDO is critical for LR (as it will be shown) and both phase and RS margins obtained with rWDO using fin control are superior than without fins (compare the green vs. blue lines).

5.2 Time-domain analysis

In the time-domain, the four closed-loop LTI systems are subjected to three different tests: (i) a 0.5 deg step command in θ_{ref} , (ii) a low-frequency, high-amplitude gust in v_w (maximum peak of 33 m/s), with a shape that is often used in the validation of launcher control systems, and (iii) high-frequency, low-amplitude gusts, generated by 100 white noise signals in n_w with different seeds. Each test is repeated for the 2^{10} corner-cases of the LFT. Results of the three tests are provided in Fig. 11a, 11b and 11c, which depict both nominal and dispersed responses of θ , \dot{z} , α , β_{TVC} , β_{fin} (from top to bottom), and observation error w_e when applicable. The latter plot also shows the actual wind gust v_w in purple.

In terms of command tracking (Fig. 11a), the first two controllers exhibit similar responses, and the main difference is a reduction of drift rate dispersion at the expense of higher TVC actuation with the blue controller. This small difference is caused by the rWDO, whose error is zero in nominal conditions, but grows in the presence of uncertainties (last row). The benefits of the rWDO become more evident in the face of both low-frequency and high-frequency wind gusts (Fig. 11b and 11c), where the induced load/AoA (third row) and drift (second row) are drastically minimised at the expense of a larger pitch angle (first row), as predicted in Sec. 3.2. In the case of high-frequency gusts, the load dispersion is alleviated by approximately 50%. The adequate operation of the rWDO is also confirmed by noting that the observation errors are significantly smaller than the actual wind, particularly for the low-frequency gust.

With the introduction of fin control (red controller), the tracking response improves profoundly as the drift caused by the TVC side-force is effectively compensated (second row of Fig. 11a), which minimises the overshoot in pitch and AoA. This compensation is also useful for wind rejection as it reduces its impact on pitch and drift (first two rows of Fig. 11b and 11c), but the induced AoA remains equivalent to the first controller (no fin control, without rWDO). The LR capabilities of the blue controller (no fin control, with rWDO) are only recovered when the rWDO is employed in combination with TVC and fins (green controller). These two controllers have very similar AoA, pitch and observation error responses in the presence of wind. However, the latter controller sees the required TVC actuation reduced (fourth row) by using minimal fin deflections (barely noticeable on the fifth row). This comes at the expense of larger tracking overshoots (Fig. 11a) compared to the red controller, but not as large as with the blue controller.

Table 2 provides an overview of the observations made throughout this section. The main objective of improving wind rejection while also enhancing phase margin and command tracking was effectively achieved with the introduction of fin control and wind disturbance observation, at the expense of a small decrease of robust stability. The insight provided by μ analysis is key when specifying the rWDO requirements – smaller observation errors will require higher observation gains in the system (recall Fig. 8a), which will result in reduced robust stability.

6. Application to Descent Flight

In this section, the generalisation of the proposed wind disturbance observation to the descent design point is showcased through the following strategies:

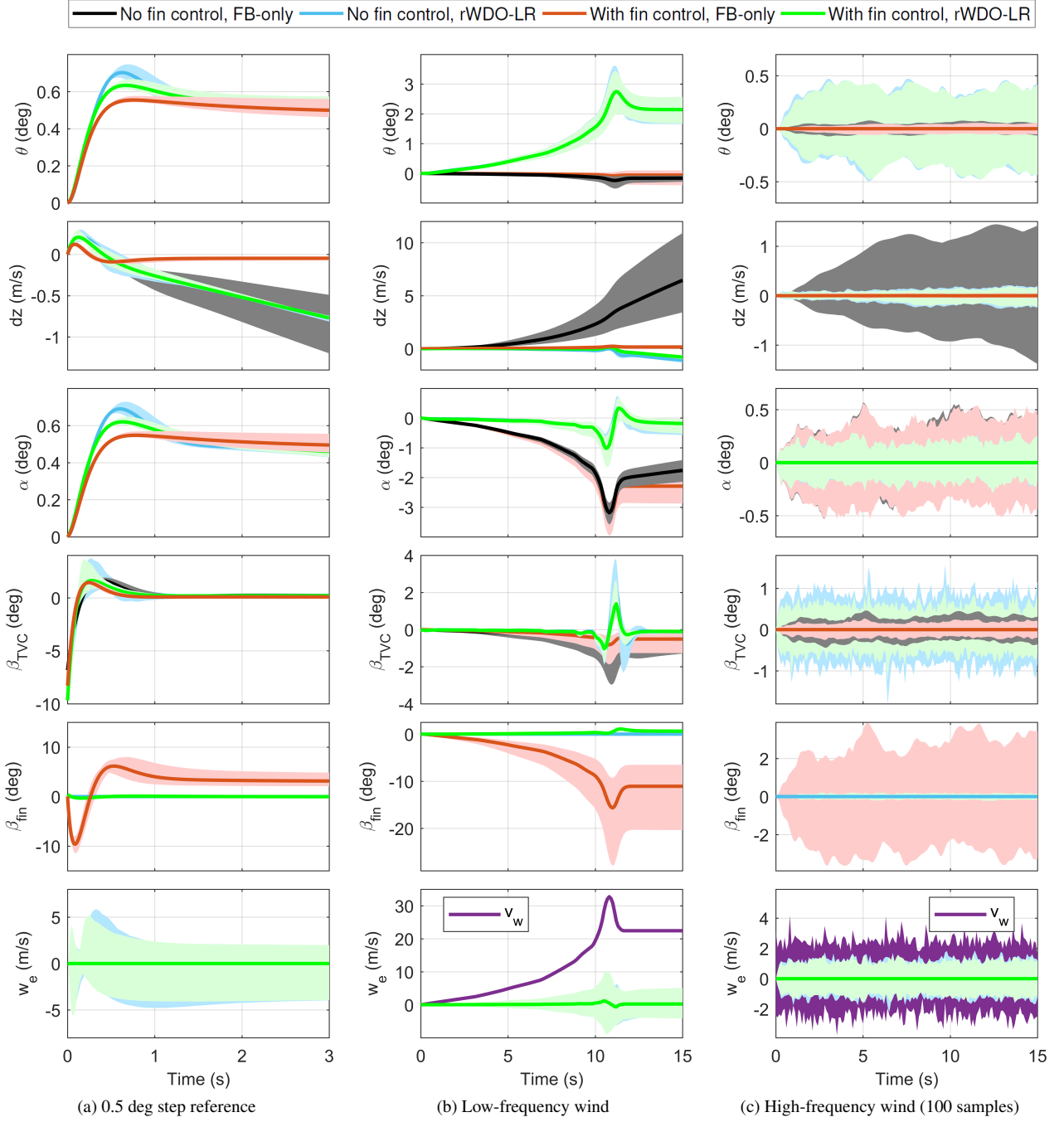


Figure 11: Monte-Carlo comparison of ascent control functionalities

Table 2: Overview of ascent control functionalities

Legend: ++ Major improvement, + Minor improvement, - Minor degradation, -- Major degradation

Fin control	rWDO load relief	Tunable gains	Phase margin	Robust stability	Command tracking	Wind rejection
No	No	3	<i>Baseline for comparison</i>			
No	Yes	3+1		--		+
Yes	No	6	++		++	
Yes	Yes	6+2	+	-	+	++

1. In black, a combined fins/TVC controller with $K_{LR}^\downarrow = \begin{bmatrix} 0 & 0 \end{bmatrix}^T$ and with K_{FB}^\downarrow tuned using structured \mathcal{H}_∞ optimisation. Using constraints on the $\theta_{ref} \rightarrow \{\theta_e, \theta, \beta_{TVC}, \beta_{fin}\}$ and $n_w \rightarrow \{\theta_e, \alpha\}$ channels, the following FB-only controller is obtained:

$$K_{FB}^\downarrow = \begin{bmatrix} -0.44 & -3.0 \times 10^{-3} & 2.5 \times 10^{-3} \\ 1.28 & 1.31 & 3.9 \times 10^{-3} \end{bmatrix} \quad (16)$$

2. In green, the controller of Eq. (16) augmented with a rWDO, which is generated by repeating the procedure of Sec. 4 for the descent design point. K_{LR}^\downarrow is chosen, as in Sec. 3.2, to be a single gain from \hat{v}_w to β_{fin} that minimises the attitude tracking error. In opposition to Sec. 5, no joint tuning of K_{FB}^\downarrow and K_{LR}^\downarrow is performed in this section.
3. In blue, a controller similar to the previous one, but in which K_{LR}^\downarrow is chosen to minimise the aerodynamic load.

The frequency and time-domain analysis of the three descent controllers is presented in Sec. 6.1 and 6.2, respectively.

6.1 Frequency-domain analysis

Having the same feedback controller K_{FB}^\downarrow , the three descent designs exhibit the same behaviour in nominal conditions, hence their frequency-domain comparison is only carried out in terms of μ analysis. The outcome of this analysis is provided in Fig. 12.

The μ analysis shows that, similar to Sec. 5.1, the introduction of the rWDO leads to an RS degradation when load is minimised (blue controller), but to an improvement when error is minimised (green controller). This is consistent with the previous observation that a better tracking performance is tightly related to better stability margins. Compared to the ascent case, the peaks of degradation are similar (maximum is $\mu = 0.49$), but take place for lower frequencies due to a value of dynamic pressure 85% smaller at the descent design point (recall Fig. 2b).

6.2 Time-domain analysis

The time-domain verification of the descent controllers is exactly the same as described in Sec. 5.2. Results of the three tests in nominal and dispersed conditions are depicted in Fig. 13a, 13b and 13c.

Focusing on command tracking first (Fig. 13a), the three cases have the same nominal response, but dispersions are smaller with the minimum error controller (green) and larger with the minimum load controller (blue), as anticipated in Sec. 6.1. In descent flight, the controllers prioritise the use of fins with respect to TVC, which is the same for the three cases as the rWDO only acts on the fin channel. The level of rWDO errors (last row) is similar to the ascent case during the three tests, since its design requirements were kept the same.

The trade-off between error and load alleviation using disturbance observation then becomes evident with the low-frequency and high-frequency wind gusts (Fig. 13b and 13c, respectively). Both figures confirm that, compared to the FB-only controller, pitch and drift errors are minimised by the green controller at the expense of larger AoA deviations in nominal and dispersed conditions, and vice-versa for the blue controller. As an example, following the 33 m/s gust (Fig. 13b), the latter controller effectively brings the steady-state AoA from 2.4 deg to zero (third row) while only worsening the pitch angle from -1.3 to -3.2 deg (first row).

The above observations highlight the benefits of the proposed WDO augmentation, introduced in Sec. 3 – control priorities can be adjusted along the mission via K_{LR} (e.g. load relief at high dynamic pressure, minimum error near touchdown), which does not affect the system's nominal stability/tracking properties and therefore does not require retuning the feedback loop.

7. Conclusions

This article has presented the development of two launcher flight control functionalities for enhanced load relief. The first one consists of augmenting a feedback-only controller with a disturbance observer for on-board wind anticipation. It is validated via an achievable performance analysis, which shows that this approach allows control priorities (e.g. minimum load vs. minimum error) to be adjusted along the mission without retuning the stabilisation/tracking feedback loop. Care must be taken when designing the wind observer as a more accurate filter results in reduced robust stability (in exchange for the higher performance obtained).

The second functionality introduces fin control in ascent flight, which significantly improves attitude tracking by counteracting the drift caused by the TVC side-force. This improvement also ameliorates the phase margin and the impact of wind on the vehicle. Based on the presented analyses, the best load relief performance is achieved by combining fin control with the wind disturbance observer.

Several disturbance observers are successfully designed and verified using robust control techniques for one point during the ascent and another one during the descent, yet the adopted framework allows to easily repeat the procedure for other points, as well as to address other effects not studied in this article (e.g. actuator, sensor, bending and sloshing dynamics).

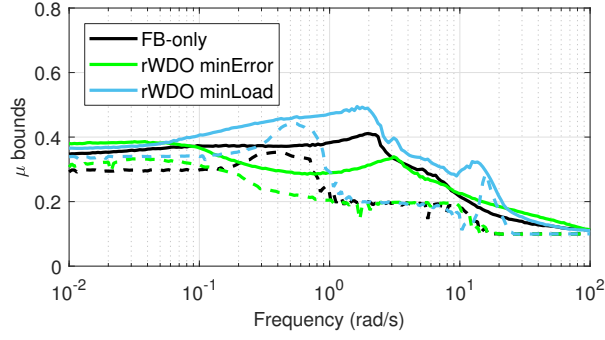


Figure 12: Robust stability upper and lower bounds of descent control functionalities

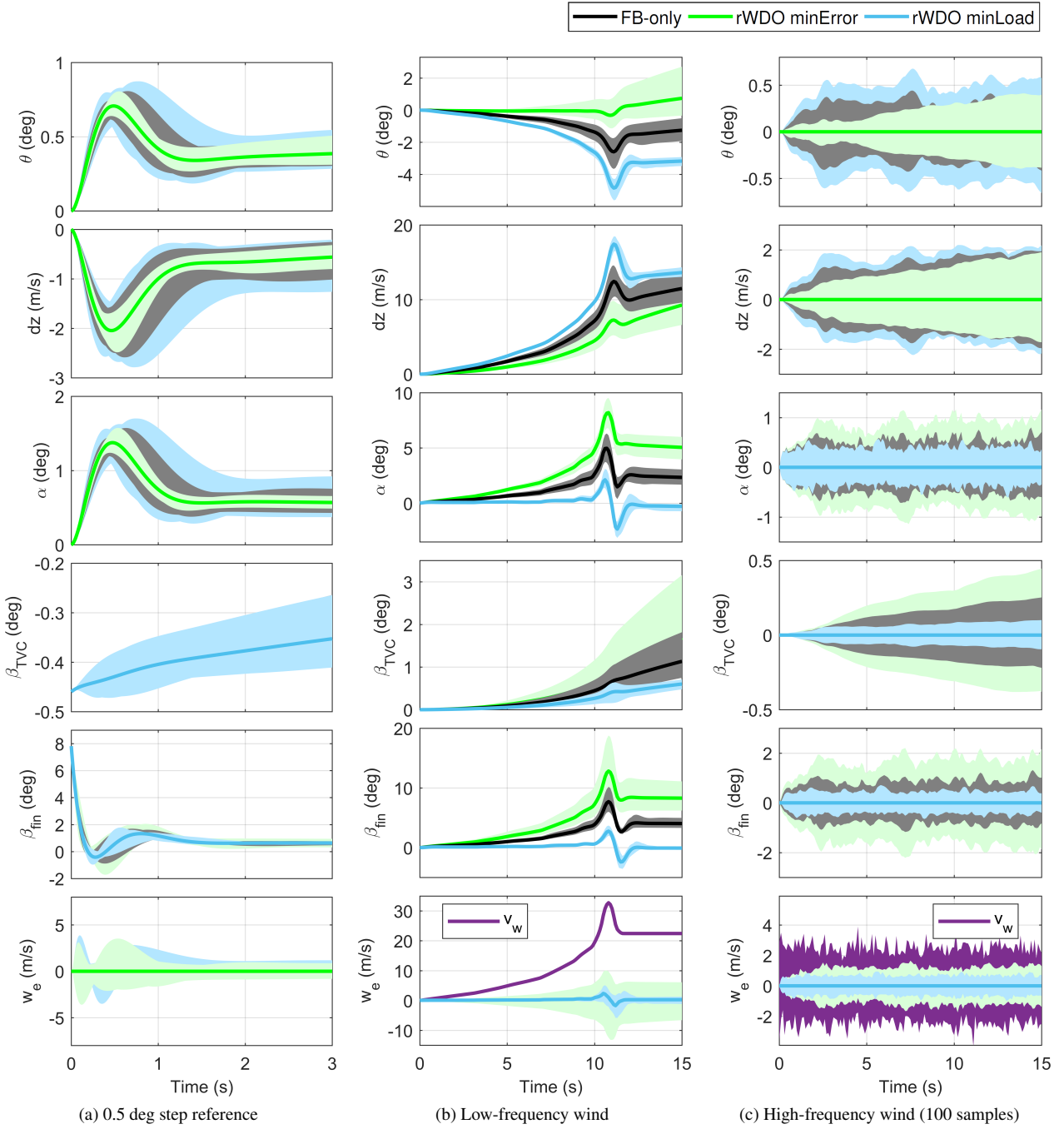


Figure 13: Monte-Carlo comparison of descent control functionalities

References

- [1] G. Balas, R. Chiang, A. Packard, and M. Safonov. *MATLAB Robust Control Toolbox User's Guide*. MathWorks, 3rd edition, 2006.
- [2] L. Blackmore. Autonomous Precision Landing of Space Rockets. *The Bridge on Frontiers of Engineering*, 4(46):15–20, 2016.
- [3] F.W. Boelitz. *Guidance, Steering, Load Relief and Control of an Asymmetric Launch Vehicle*. Master's thesis, Massachusetts Institute of Technology, August 1989.
- [4] F.W. Boelitz. Kistler launch assist platform return burn control. In *The 1999 AIAA Guidance, Navigation, and Control Conference and Exhibit*, Portland, OR, Aug 9–11 1999.
- [5] F.W. Boelitz, L. Singh, C.M. Gibson, S.R. Smith, P. Miotto, and A.A. Martin. *Load Relief System for a Launch Vehicle*. US Patent 6,666,410, 2003.
- [6] J. Bradford, B. Germain, and K. Feld. Optimization of a Reusable Rocket-Powered, VTVL Launch System: A Case Study of the Falcon 9-R. *SpaceWorks Case Study*, Aug 2014.
- [7] R. Caverly, J. Forbes, B. Danowsky, and P. Suh. Gust-Load Alleviation of a Flexible Aircraft using a Disturbance Observer. In *The AIAA SciTech 2017 Forum*, Grapevine, TX, Jan 9–13 2017.
- [8] E. Dumont, S. Stappert, T. Ecker, J. Wilken, S. Karl, S. Krummen, and M. Sippel. Evaluation of Future Ariane Reusable VTOL Booster Stages. In *The 68th International Astronautical Congress*, Adelaide, Sep 25–29 2017.
- [9] N. Fezans, H.-D. Joos, and C. Deiler. Gust load alleviation for a long-range aircraft with and without anticipation. *CEAS Aeronautical Journal*, Early View, 2019.
- [10] R.F. Hoelker. *Theory of Artificial Stabilization of Missiles and Space Vehicles with Exposition of Four Control Principles*. NASA TN D-55, June 1961.
- [11] A. Kumar, E. Bossanyi, and A. Scholbrock et al. Field Testing of LiDAR Assisted Feedforward Control Algorithms for Improved Speed Control and Fatigue Load Reduction. In *The 2015 EWEA Event*, Paris, 2015.
- [12] J. Livingston and J. Redus. Load-reducing flight control systems for the Saturn V with various payloads. In *The 1968 AIAA Control and Flight Dynamics Conference*, Pasadena, CA, Aug 12–14 1968.
- [13] A.A. Martin. *Model Predictive Control for Ascent Load Management of a Reusable Launch Vehicle*. Master's thesis, Massachusetts Institute of Technology, June 2002.
- [14] D. Navarro-Tapia, A. Marcos, P. Simplício, S. Bennani, and C. Roux. Legacy Recovery and Robust Augmentation Structured Design for the VEGA Launcher. *International Journal of Robust and Nonlinear Control*, 29(11), 2019.
- [15] J. Orr and T. VanZwieten. Robust, Practical Adaptive Control for Launch Vehicles. In *The 2012 AIAA Guidance, Navigation, and Control Conference*, Minneapolis, MN, Aug 13–16 2012.
- [16] D. Ossmann and C. Poussot-Vassal. Design and Assessment of a Two Degree of Freedom Gust Load Alleviation System. In *The 5th CEAS EuroGNC Conference*, Milan, Italy, Apr 3–5 2019.
- [17] P. Simplício, S. Bennani, A. Marcos, C. Roux, and X. Lefort. Structured Singular-Value Analysis of the Vega Launcher in Atmospheric Flight. *Journal of Guidance, Control, and Dynamics*, 39(6):1342–1355, 2016.
- [18] P. Simplício, A. Marcos, and S. Bennani. Guidance of Reusable Launchers: Improving Descent and Landing Performance. *submitted to the Journal of Guidance, Control, and Dynamics*, 2019.
- [19] P. Simplício, A. Marcos, and S. Bennani. Reusable Launchers: Development of a Coupled Flight Mechanics, Guidance and Control Benchmark. *submitted to the Journal of Spacecraft and Rockets*, 2019.
- [20] M. Sippel, S. Stappert, L. Bussler, and E. Dumont. Systematic Assessment of Reusable First-Stage Return Options. In *The 68th International Astronautical Congress*, Adelaide, Australia, Sep 25–29 2017.
- [21] H. Suzuki. Load Relief Control of H-IIA Launch Vehicle. In *The 16th IFAC Symposium on Automatic Control in Aerospace*, Saint-Petersburg, Russia, Jun 14–18 2004.
- [22] R. Takase, Y. Hamada, and T. Shimomura. Aircraft Gust Alleviation Preview Control with a Discrete-Time LPV Model. *Journal of Control, Measurement, and System Integration*, 11(3):190–197, 2018.
- [23] P. Tartabini, J. Beaty, R. Lepsch, and M. Gilbert. *Payload Performance Analysis for a Reusable Two-Stage-to-Orbit Vehicle*. NASA Technical Reports Server, May 2015.
- [24] P. Towers and B. Jones. Real-time wind field reconstruction from LiDAR measurements using a dynamic wind model and state estimation. *Wind Energy*, 19:133–150, 2016.
- [25] B. Wie, W. Du, and M. Whorton. Analysis and Design of Launch Vehicle Flight Control Systems. In *The 2008 AIAA Guidance, Navigation, and Control Conference and Exhibit*, Honolulu, HI, Aug 18–21 2008.